

Supplementary Materials for

**Noninvasive measurement of local stress inside soft materials with
programmed shear waves**

Zhaoyi Zhang *et al.*

Corresponding author: Yanping Cao, caoyanping@tsinghua.edu.cn; Guo-Yang Li, gli26@mgh.harvard.edu

Sci. Adv. **9**, eadd4082 (2023)
DOI: 10.1126/sciadv.add4082

The PDF file includes:

Supplementary notes S1 to S5
Figs. S1 to S8
Legends for movies S1 and S2
References

Other Supplementary Material for this manuscript includes the following:

Movies S1 and S2

Supplementary Note 1: The stress identity

Here we prove the following identity, used in the paper to connect wave speeds with stress:

$$\sigma_{11} - \sigma_{33} = \mathcal{A}_{1313}^0 - \mathcal{A}_{3131}^0. \quad (\text{S-1})$$

In the paper we write these moduli as $\alpha = \mathcal{A}_{1313}^0$ and $\gamma = \mathcal{A}_{3131}^0$, and considered scenarios where the components of the Cauchy stress σ_{11} and σ_{33} are the principal stresses σ_1 and σ_3 , respectively. Here \mathcal{A}_{piqj}^0 are the Cartesian components of the Eulerian elasticity tensor. For incompressible solids, they are determined from the strain energy function W and the deformation gradient tensor with components F_{iJ} as (28, 50)

$$\mathcal{A}_{piqj}^0 = (\sigma_{pq} + \bar{p}\delta_{pq})\delta_{ij} + 4F_{pP}F_{qQ}\frac{\partial^2 W}{\partial C_{IP}C_{QJ}}F_{il}F_{jJ}, \quad (\text{S-2})$$

where $C_{IJ} = F_{kI}F_{kJ}$, summation over repeated indices is implied, and δ_{ij} is the Kronecker delta.

Hence

$$\mathcal{A}_{1313}^0 = \sigma_{11} + \bar{p} + 4F_{1P}F_{1Q}\frac{\partial^2 W}{\partial C_{IP}C_{QJ}}F_{3I}F_{3J}, \quad (\text{S-3})$$

$$\mathcal{A}_{3131}^0 = \sigma_{33} + \bar{p} + 4F_{3P}F_{3Q}\frac{\partial^2 W}{\partial C_{IP}C_{QJ}}F_{1I}F_{1J} = \sigma_{33} + \bar{p} + 4F_{1P}F_{1Q}\frac{\partial^2 W}{\partial C_{IP}C_{QJ}}F_{3I}F_{3J}, \quad (\text{S-4})$$

where for the last equation we swapped the dummy variables $I \leftrightarrow P$ and $Q \leftrightarrow J$, and then we used the symmetries $C_{IP} = C_{PI}$. By subtraction we obtain the identity (S-1).

Often the stress is modeled as being caused by a finite elastic deformation from a stress-free configuration. When instead, we consider small elastic waves in an initially stressed reference where the initial stress, denoted by τ_{ij} is due to *any origin*, then in the above we would take $F_{pP} = \delta_{pP}$ (28, 29), and the identity would still hold.

For future reference, we recall that the Cauchy stress is computed as (50)

$$\sigma_{ij} = F_{iK}\frac{\partial W}{\partial F_{jK}} - \bar{p}\delta_{ij}, \quad (\text{S-5})$$

where \bar{p} is a Lagrange multiplier due to the constraint of incompressibility.

Supplementary Note 2: Phase and group velocity

Here we relate the wave speeds to the moduli appearing in the stress identity (S-1).

We start with the equation of motion for plane shear waves of the form $\mathbf{u} = \mathbf{u}_0 e^{ik(\mathbf{n} \cdot \mathbf{x} - vt)}$, which is given by Equation (5.16) in Ref. (51):

$$(\mathbf{I} - \mathbf{n}\mathbf{n}^T)\mathbf{Q}(\mathbf{n})(\mathbf{I} - \mathbf{n}\mathbf{n}^T)\mathbf{u}_0 = \rho v^2 \mathbf{u}_0, \quad (\text{S-6})$$

where $\mathbf{x} = (x_1, x_2, x_3)$, $\mathbf{n} = (n_1, n_2, n_3)$, $Q_{ij}(\mathbf{n}) = \mathcal{A}_{piqj}^0 n_p n_q$, and \mathbf{u}_0 is a unit vector along the direction of polarization (orthogonal to \mathbf{n} , the unit vector along the direction of propagation).

Then its wave speed v is given by

$$\rho v^2 = \mathbf{u}_0^T \mathbf{Q}(\mathbf{n}) \mathbf{u}_0. \quad (\text{S-7})$$

Let v_x and v_z be the speeds of the shear waves when $\mathbf{n} = (1, 0, 0)$, $\mathbf{u}_0 = (0, 0, 1)$, and $\mathbf{n} = (0, 0, 1)$, $\mathbf{u}_0 = (1, 0, 0)$, respectively. From the above it follows that

$$\rho v_x^2 = \mathcal{A}_{1313}^0, \quad \rho v_z^2 = \mathcal{A}_{3131}^0. \quad (\text{S-8})$$

To guarantee that there are two shear waves with speeds (S-8) that satisfy the equation of motion (S-6), we assume that all forms of anisotropy are coaxial with the deformation tensor $\mathbf{C} = \mathbf{F}\mathbf{F}^T$. Different types of anisotropy, such as the ones captured by an initial stress tensor $\boldsymbol{\tau}$ (28–30) or a structural anisotropy tensor $\mathbf{M}\mathbf{M}^T$ (where \mathbf{M} is a unit vector along the preferred direction in the reference configuration for transversely isotropic materials, see for example Ref. (51)), can be included in the strain-energy W , from which we can deduce the moduli \mathcal{A}_{piqj}^0 with (S-2). For example, $\boldsymbol{\tau}$ and $\mathbf{M}\mathbf{M}^T$ are coaxial with \mathbf{C} , and themselves, when

$$\mathbf{C}\boldsymbol{\tau} = \boldsymbol{\tau}\mathbf{C}, \quad \mathbf{C}\mathbf{M}\mathbf{M}^T = \mathbf{M}\mathbf{M}^T\mathbf{C}, \quad \text{and} \quad \boldsymbol{\tau}\mathbf{M}\mathbf{M}^T = \mathbf{M}\mathbf{M}^T\boldsymbol{\tau}.$$

This condition implies, for example, that \mathbf{M} is aligned with the principal directions of the initial stress $\boldsymbol{\tau}$ and the final stress $\boldsymbol{\sigma}$.

In more detail, W can be written as a sum and multiplication of terms of the form $\text{tr}(\mathbf{A}\mathbf{C}^n\mathbf{B})$ for integer n where \mathbf{A} and \mathbf{B} are some multiplication of anisotropy tensors such as $\boldsymbol{\tau}$ and $\mathbf{M}\mathbf{M}^T$. When all these tensors are coaxial, and we choose a coordinate system aligned with their axes, we find that

$$\mathcal{A}_{piqj}^0 = 0 \quad \text{unless} \quad \begin{cases} p = i \& q = j, & \text{or} \\ p = q \& i = j, & \text{or} \\ p = j \& q = i. \end{cases} \quad (\text{S-9})$$

By assuming the above, we can deduce which elastic shear waves can give us access to the stress identity (S-1).

Let $\mathbf{n} = (\cos \theta, \sin \theta, 0)$ and $\mathbf{u}_0 = (-\sin \theta, \cos \theta, 0)$, which substituted into (S-7) leads to

$$\rho v^2 = \alpha \cos^4 \theta + 2\beta \cos^2 \theta \sin^2 \theta + \gamma \sin^4 \theta, \quad (\text{S-10})$$

where the moduli α, β, γ are defined as $\alpha = \mathcal{A}_{1313}^0$, $2\beta = \mathcal{A}_{1111}^0 + \mathcal{A}_{3333}^0 - 2\mathcal{A}_{1133}^0 - 2\mathcal{A}_{3113}^0$, $\gamma = \mathcal{A}_{3131}^0$. Note this is the same result as deduced in (25, 50, 52) with the difference that here we showed that it holds in general when (S-9) holds. This justifies how and when our method applies to anisotropic solids under stress.

Now consider two shear waves, one with propagation direction $\theta = \theta_0$ and the other with $\theta = \pm\pi/2 \pm \theta_0$ with the speeds v_x and v_z , respectively. Then, according to Eq. (S-10) and (S-1), we find that

$$\sigma_1 - \sigma_3 = \rho \frac{v_x^2 - v_z^2}{\cos 2\theta_0}, \quad (\text{S-11})$$

a generalization of the result established in (25) for isotropic solids.

The group velocities \mathbf{v}_g are often easier to measure in shear wave elastography experiments, in comparison to the phase speed given by Eq. (S-10). The group velocity depends on the anisotropy of the material, and the initial forcing of the wave (34), what we call the Acoustic Radiation Force (ARF). For the ARF we programmed, as shown in Fig. 2 and Fig. S2, we were able to generate waves propagating along the x and z directions whose wavefronts are locally

flat. In these cases, the phase velocity can be measured, so in conclusion we can use Eq. (S-10). However, it is certainly easier to generate a point ARF. So we also discuss this case.

For an ARF focused on one point that equally excites bulk waves in all directions, the group velocity is given by $v_g = \partial(kv)/\partial k$ (34), where $k = k\mathbf{n}$ denotes the wave vector. For the phase velocity v given by Eq. (S-10) we obtain the group velocities:

$$v_{g1} = \frac{\alpha \cos \theta + (2\beta - \alpha - \gamma) \sin^4 \theta \cos \theta}{\rho v}, \quad (\text{S-12})$$

and

$$v_{g3} = \frac{\gamma \sin \theta + (2\beta - \alpha - \gamma) \sin \theta \cos^4 \theta}{\rho v}. \quad (\text{S-13})$$

Equations (S-12) and (S-13) show that the phase and group speed are identical in the principal directions $\theta = 0$ and $\pi/2$, because there, $\rho v^2 = \alpha, \gamma$, respectively. The coincidence of the two speeds along and at the right angle to the axis of symmetry always holds, see (53, p.16) for example. For isotropic materials subject to moderate stress we have the further simplification $2\beta \approx \alpha + \gamma$ (52), which results in

$$\rho v^2 = \alpha \cos^2 \theta + \gamma \sin^2 \theta, \quad v_{g1} = \frac{\alpha \cos \theta}{\rho v}, \quad v_{g3} = \frac{\gamma \sin \theta}{\rho v}, \quad (\text{S-14})$$

and thus

$$\frac{v_{g1}^2}{\alpha/\rho} + \frac{v_{g3}^2}{\gamma/\rho} = 1, \quad (\text{S-15})$$

which describes an elliptical wavefront. This elliptical wavefront has also been revealed by Rouze et al. (34) in the case of the Mooney-Rivlin material, where $2\beta = \alpha + \gamma$ always holds regardless of the stress level. However, for other constitutive models such as the Arruda–Boyce model, Rouze et al. (34) show that cusp structures in wavefront may emerge in isotropic materials when sufficiently large stress is applied. These cusps are usually induced by structural anisotropy of materials, as shown in Fig. S1.

For experiments where only the group velocities are available (which is not our case), it would be necessary to first calculate the phase velocities from the measured group velocities.

Supplementary Note 3: Measurement of the lateral shear wave speed

We performed two-dimensional Fourier transforms on Fig. S4A to get the frequency-wavenumber domain data, as shown in Fig. S4B. To identify the left-to-right (LR) shear waves, we performed an inverse Fourier transform to the data in the first and third quadrants (and set the data points in the second and fourth quadrants to zero), as shown in Fig. S4C. Similarly, the right-to-left (RL) shear waves were obtained by inverse Fourier transform on the data in the second and fourth quadrants (Fig. S4D).

We then performed Radon transformations to the spatiotemporal data to obtain the shear wave group velocity. The Radon transform sums the intensity of pixels in a spatiotemporal map along projections with different slopes (denoted by $\tan \Theta$) and intercepts. The optimal projection is identified by the peak Radon sum (41). For the lateral shear waves, the six wavefronts induced by the six ARF pushes are parallel, resulting in multiple peaks in the Radon sum (Figs. S4E and F). Therefore, we summed the absolute values of the Radon sums obtained from the projections with the same slopes (each column of the Radon sums), as shown in Figs. S4G and H. We identified the maxima in Figs. S4G and H, respectively, to get the group velocities of the LR and RL shear waves, i.e., $\sim |\tan 67^\circ| \frac{\Delta x}{\Delta t}$ and $\sim |\tan 113^\circ| \frac{\Delta x}{\Delta t}$, respectively, where $\Delta x = 0.1$ mm and $\Delta t = 0.1$ ms are the grid size of spatiotemporal maps. Finally we reported the average of the two optical group velocities as the value of v_x .

Supplementary Note 4: Hydrogel sample characterization

The hydrogel consists of 10% polyvinyl alcohol (PVA), 3% cellulose and 87% deionized water by weights. We dissolved the PVA powder (sigma Aldrich 341584, Shanghai, China) into 80°C water. We then added cellulose powder (Sigma-Aldrich S3504, Shanghai, China) into the solution and fully stirred the solution to get a suspension of the cellulose powder. The cellulose particles act as ultrasonic scatterers to enhance the imaging contrast. We poured the suspension into a square plastic box (length ~ 30 cm, width ~ 7 cm, and height ~ 4 cm), and then cooled the suspension to room temperature (~ 20°C) before putting it into a -20°C freezer. We froze the sample for 12 hours and then thawed it at room temperature for another 12 hours. The stiffness of the sample can be tuned by the freezing/thawing (F/W) cycles (49). The hydrogel sample used in this study underwent two F/W cycles.

We performed indentation tests (Fig. S5A) to characterize the viscoelastic properties of the hydrogel sample. To get the long-term modulus, we performed three indentation tests using a low loading rate (~ 0.1 mm/s), as shown in Fig. S5B. The long-term shear modulus $\mu_\infty = \mu(t \rightarrow +\infty)$ can be obtained by fitting the loading curve with the formula

$$F = \frac{16}{9} \mu_\infty R^{1/2} h^{3/2}, \quad (\text{S-16})$$

where $R \approx 7.5$ mm is the radius of the indenter, F is the force, and h is the indentation depth. As shown in Fig. S5B, the best fitting gives $\mu_\infty = 8.6 \pm 0.3$ kPa. We then increased the loading rate (~ 100 mm/s) and measured the stress relaxation when holding the indentation depth at ~ 5 mm. Figure S5C shows the normalized stress relaxation curve. We find the two-term Prony series with $g_1 = 0.07$, $\tau_1 = 0.08$ s, $g_2 = 0.05$ and $\tau_2 = 2.05$ s fits the stress relaxation data well. The total stress relaxation is small ($g_1 + g_2 \approx 10\%$), indicating a weak viscosity of the hydrogel sample, which only introduces a ~ 5% variation in shear wave speed over the frequency range from ~ 0.5 Hz (τ_2^{-1}) to ~ 12.5 Hz (τ_1^{-1}).

While the stress relaxation characterizes the viscoelasticity in the low frequency regime (below ~ 12.5 Hz), we further measured the surface wave phase velocity up to 800 Hz using our ultrasound elastography system. In this measurement, we relied on a mechanical shaker (SA-JZ002, Shiao, Jiangsu, China) to apply a surface pressure locally to generate harmonic surface waves. The surface waves were acquired by the ultrasound transducer. We then computed the wavelengths of the surface waves to get the phase velocity. As shown in Fig. S5D, interestingly, we do not observe an increase in the speed, but instead a slight decrease. We attribute this decrease to the slight stiffness gradient (softer at shallower locations) of the hydrogel sample introduced by the fabrication process (54). Despite the slight material heterogeneity, the dispersion relation suggests a weak dependence of the surface wave speed on the frequency, indicating a weak viscosity of the hydrogel in the frequency range of 100 to 800 Hz.

Supplementary Note 5: Acoustoelastic model for skeletal muscle and the effect of viscoelasticity

Linear elastic parameters

To characterize the anisotropy of the skeletal muscle, we measured the shear wave group velocities along different directions. Our main assumption is that the skeletal muscle can be modeled as an incompressible transversely isotropic material due to a preferred direction of the muscle fibers. Such a material has three independent elastic parameters, say μ_T , the transverse shear modulus, μ_L , the longitudinal shear modulus, and E_L , the longitudinal Young modulus.

We measured the horizontal shear wave speeds v_x in the undeformed material at three different orientations of the fibers with respect to the x axis ($0, 35, 90^\circ$, see Figs. S4a-c) to get $v_x^{0^\circ}$, $v_x^{35^\circ}$, and $v_x^{90^\circ}$. Then the three elastic parameters can be calculated by the formulas (51)

$$\mu_T = \rho(v_x^{90^\circ})^2, \quad \mu_L = \rho(v_x^{0^\circ})^2, \quad E_L = \frac{4 [\rho(v_x^{35^\circ})^2 - \mu_L]}{\sin^2(2 \times 35^\circ)} + (4\mu_L - \mu_T). \quad (\text{S-17})$$

Figure S6 shows the statistical results for the shear wave speeds, which clearly point to the mechanical anisotropy of the muscle. From the wave speeds we get $\mu_T \approx 10.7$ kPa, $\mu_L \approx 22.4$ kPa, and $E_L \approx 40.1$ kPa.

Acoustoelastic model for skeletal muscle

To model the acoustoelasticity of the skeletal muscle, we take the phenomenological model proposed by Murphy (55),

$$W = \frac{\mu_T}{2c_2} [e^{c_2(I_1-3)} - 1] + \frac{E_L + \mu_T - 4\mu_L}{2c_4} [e^{c_4(\sqrt{I_4}-3)} - 1] + \frac{\mu_T - \mu_L}{2} (2I_4 - I_5 - 1), \quad (\text{S-18})$$

where c_2 and c_4 are non-dimensional strain-hardening parameters, and the strain invariants are defined as

$$I_1 = \text{tr } \mathbf{C}, \quad I_2 = \frac{1}{2}[I_1^2 - \text{tr}(\mathbf{C}^2)], \quad I_4 = \mathbf{M} \cdot (\mathbf{C}\mathbf{M}), \quad I_5 = \mathbf{M} \cdot (\mathbf{C}^2\mathbf{M}). \quad (\text{S-19})$$

This model reduces to the neo-Hookean model,

$$W = \mu(I_1 - 3), \quad (\text{S-20})$$

when we take $\mu_T = \mu_L = \frac{1}{3}E_L = \mu$ and $c_2 = 0$.

Inserting (S-18) into (S-2) we obtain the expressions for α , β , and γ , which determine the shear wave speed according to Eq. (1) in the main text. When $\mathbf{M} = (1, 0, 0)$, we find

$$\begin{aligned} \rho v^2 &= \mu_T \lambda^2 \sin^2 \theta e^{c_2(I_1-3)} + \lambda^{-1} \cos^2 \theta \left[\mu_T e^{c_2(I_1-3)} + (\mu_T - \mu_L)(2 - 3\lambda^{-1}) \right] \\ &\quad + \lambda^{-1} \cos^2 \theta \left[(E_L + \mu_T - 4\mu_L) e^{c_4(\lambda-1)^2} (1 - \lambda^{-1}) \right], \end{aligned} \quad (\text{S-21})$$

where $I_1 = \lambda^2 + 2\lambda^{-1}$, and λ is the stretch ratio along the direction of tension, obtained by solving

$$\begin{aligned} \sigma_1 &= \lambda \left[\mu_T \lambda e^{c_2(I_1-3)} + (E_L + \mu_T - 4\mu_L)(\lambda - 1) e^{c_4(\lambda-1)^2} + 2(\mu_T - \mu_L)(\lambda - \lambda^3) \right] \\ &\quad - \frac{\mu_T}{\lambda} e^{c_2(I_1-3)}, \end{aligned} \quad (\text{S-22})$$

given the principal stress σ_1 . Figure S1 shows the typical dependence of the wave speed on direction when the material is subject to a uni-axial tension.

Inserting $\mu_T = 10.7$ kPa, $\mu_L = 22.4$ kPa, and $E_L = 40.1$ kPa into Eq. (S-21), and then using this equation to fit $v_x(\theta = 0)$ and $v_z(\theta = \pi/2)$ shown in Fig. 4d, we get $c_2 \approx 3.5$ and $c_4 \approx 8$. The fitting curves are shown in Fig. 4d of the main text.

Viscoelasticity of the skeletal muscle and its effect on shear wave propagation

The dispersion relation of the Rayleigh surface wave in the muscle sample was measured using the same setup as described in Note 4. Figure S4E shows the surface wave speeds measured along the muscle fiber. We fit the dispersion relation with a one-term Prony series, to get $g_1 \approx 0.79$ and $\tau_1 \approx 0.49$ ms.

To evaluate the effect of the viscoelasticity on the acoustoelastic imaging, we use the acousto-visco-elastic model recently proposed by Benjamin and de Pascalis (46). For simplicity, we

consider the quasi-linear viscoelasticity (QLV) theory with the neo-Hookean model (Eq. (S-20)) and a one-term Prony series. According to (46), the shear wave speed v_x is a function of the frequency f ,

$$v_x = \sqrt{\frac{2(1+D^2)}{1+\sqrt{1+D^2}}} \sqrt{\frac{|\operatorname{Re} \mu_x|}{\rho}} \quad (\text{S-23})$$

where

$$\begin{aligned} D &= D_0 \frac{2\Omega\Omega_0}{\Omega^2 + \Omega_0^2}, & \Omega &= 2\pi f \tau_1, \\ D_0 &= \frac{g}{2\Omega_0} \frac{\bar{\mu}_x^v}{\bar{\mu}_x^v + (1-g)[\bar{T}_d^e]_{11}}, & \Omega_0^2 &= (1-g) \frac{\bar{\mu}_x^v + [\bar{T}_d^e]_{11}}{\bar{\mu}_x^v + (1-g)[\bar{T}_d^e]_{11}}, \end{aligned} \quad (\text{S-24})$$

and

$$\mu_x = (1-g_1)[\bar{T}_d^e]_{11} + (1 - \frac{g_1}{1+i\omega\tau_1})\bar{\mu}_x^v. \quad (\text{S-25})$$

In (S-24) and (S-25), $i = \sqrt{-1}$,

$$[\bar{T}_d^e]_{11} = \mu(\lambda^2 - I_1/3), \quad \bar{\mu}_x^v = \mu I_1/3. \quad (\text{S-26})$$

and λ is the stretch ratio, which can be determined from the stress σ_1 by solving the cubic

$$\lambda^3 - \frac{\sigma_1}{\mu_\infty}\lambda - 1 = 0, \quad (\text{S-27})$$

where $\mu_\infty = \mu(\infty) = (1-g_1)\mu_0$ is the long-term shear modulus and $I_1 = \lambda^2 + 2\lambda^{-1}$. To get v_z , we follow the same procedure, replacing λ with $\lambda^{-1/2}$ in (S-26).

In Fig. S7, we plot the dispersion relations of v_x and v_z with $\mu_\infty = 8.4$ kPa, $g_1 = 0.79$ and $\tau_1 = 0.49$ ms. Then we use Eq. (2) in the main text to derive the stress σ_1 . As shown in Fig. S7B, the stress is underestimated when the viscoelasticity comes into play.

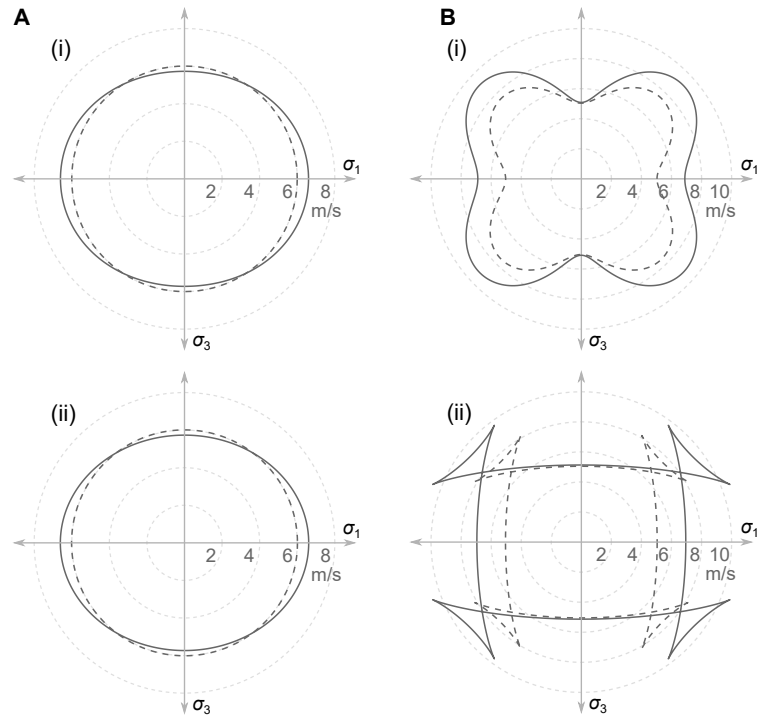


Fig. S1: Effect of the uniaxial stress on the shear wave speeds. (A) neo-Hookean material with shear modulus $\mu = 36$ kPa, subject to uniaxial stress $\sigma_1 = 0.3\mu$. (B) Transversely isotropic material with material parameters $\mu_T = 9$ kPa, $\mu_L = 25$ kPa, $E_L = 216$ kPa, $c_1 = 1$, $c_2 = 10$, and $\sigma_1/E_L = 0.1$. The fiber direction is aligned with x_1 . (i) and (ii) depict phase and group speeds, respectively, showing that they are the same along the principal axes. Solid lines: prestressed. Dashed lines: stress-free.

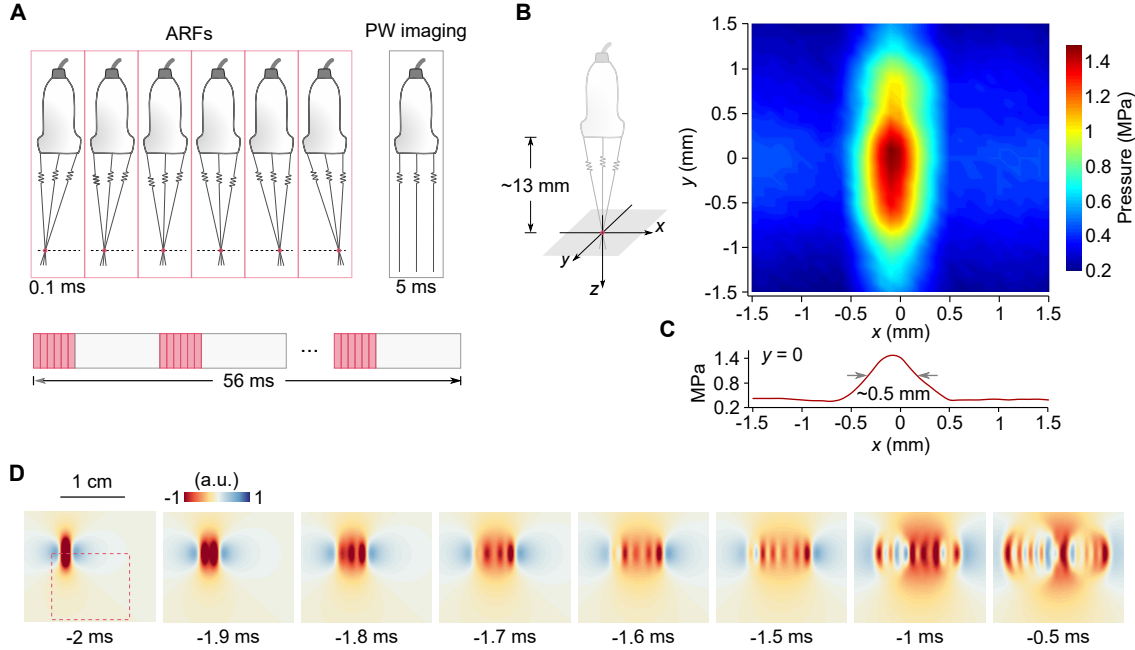


Fig. S2: Imaging protocol and finite element simulation of shear wave excitation. (A) Imaging protocol. Six ARFs are applied by successively focusing the ultrasound beam along the horizontal direction. The duration of each ARF is ~ 0.1 ms. After the excitation (~ 0.6 ms), the transducer is switched to perform plane wave (PW) imaging (unfocused beam, duration 5 ms) at a frame rate of 10 kHz. Ten successive measurements (~ 56 ms) are performed and then the average of the measurements is taken to improve the signal-to-noise ratio. (B) Acoustic pressure of the focused ultrasound beam measured within the focal plane (~ 13 mm away from the transducer). (C) Distribution of the pressure along x axis. Half width at half maximum (HWHM) is approximately ~ 0.25 mm, in agreement with the ultrasound wavelength ~ 0.23 mm. (D) Finite element simulations showing the six ARFs successively applied to excite the shear waves. The time when the PW imaging starts is set to 0. The dashed square shows the region of interest where the wave propagation is measured by the PW imaging.

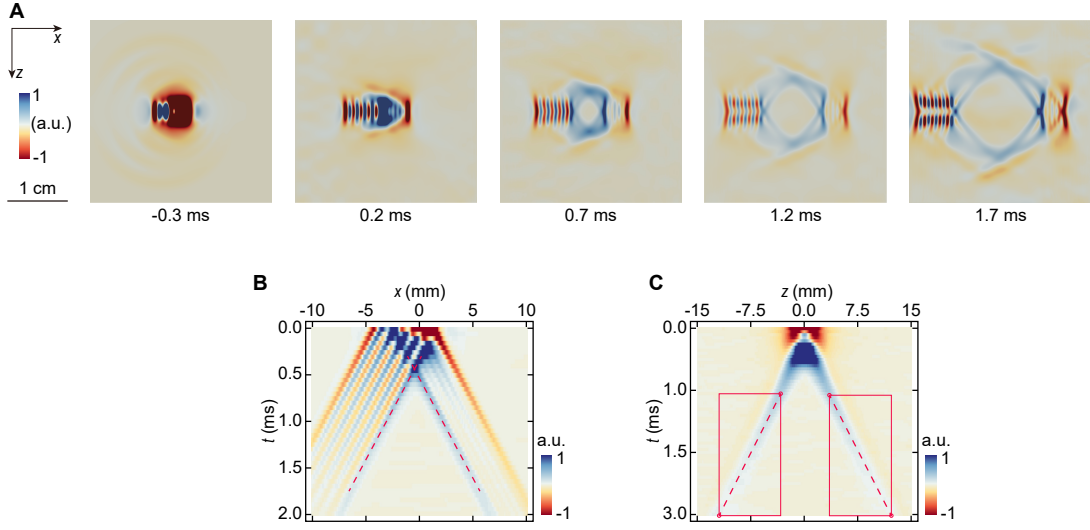


Fig. S3: Finite element simulation of the shear wave excitation by programmed acoustic radiation forces in anisotropic materials. (A) The snapshots of the shear wave propagation, which suggest the SV shear waves are primarily excited. The maps depict the vertical particle velocity fields. (B) and (C) Spatiotemporal data for the horizontal and vertical waves, respectively. The speeds measured along the two directions are identical, ~ 4.7 m/s ($\sqrt{\mu_L/\rho}$), indicating the SV shear waves are measured in both directions. The material is incompressible transversely isotropic. The fiber direction is aligned with x . The material parameters used in the simulation are $\mu_T = 10.7$ kPa, $\mu_L = 22.4$ kPa, $E_L = 40.1$ kPa, and $\rho = 1000$ kg/m³ (see Note 5 for definitions of the material parameters).

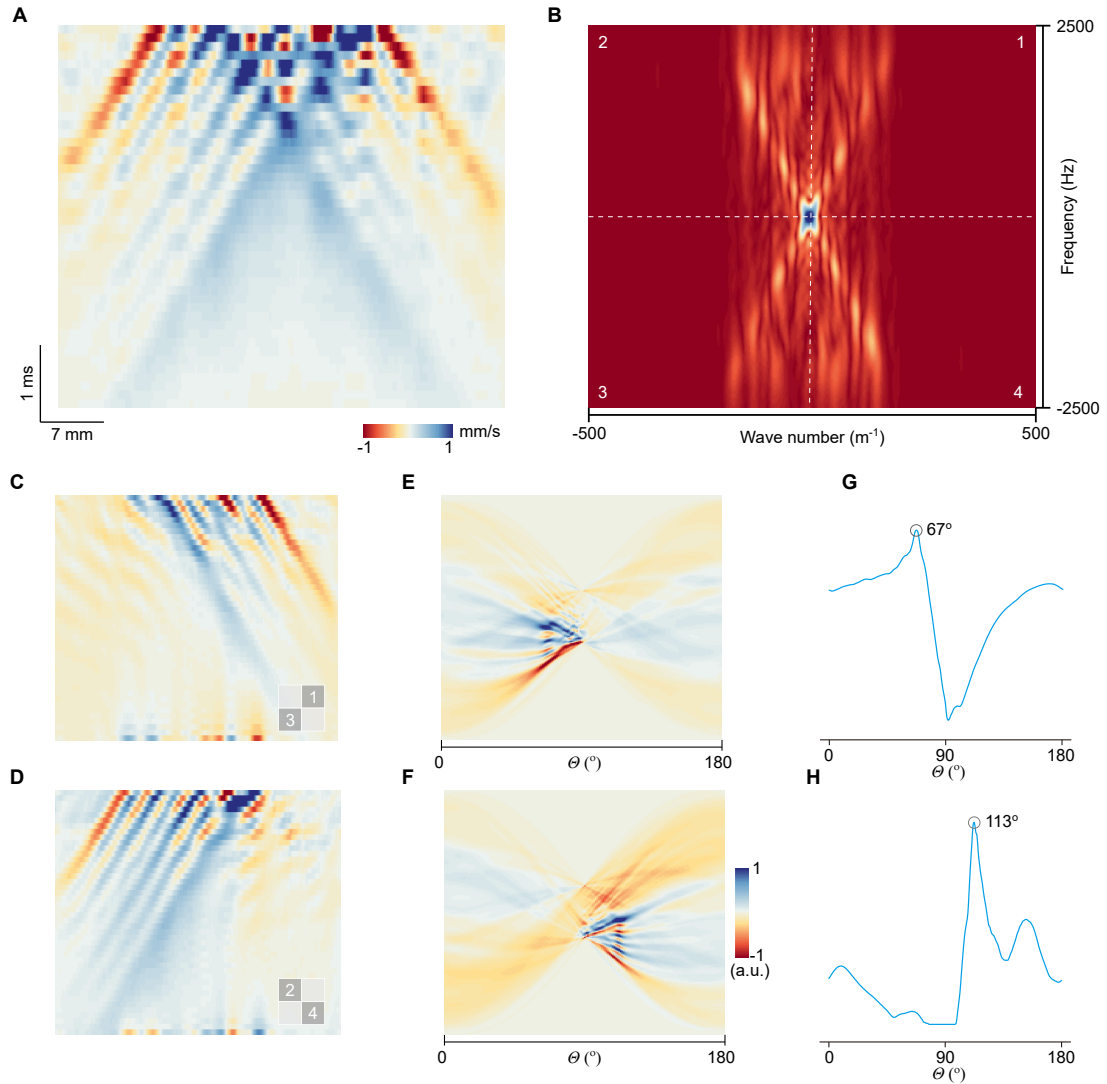


Fig. S4: Measurement of the lateral shear wave speed v_x . (A) Spatiotemporal map of the shear waves propagating along the horizontal direction (x axis). (B) Fourier transformation of the spatiotemporal data. (C) Inverse Fourier transformation of the data in the first and third quadrants. The right-to-left (RL) waves have been filtered out in this map. (D) Inverse Fourier transformation of the data in the second and fourth quadrants. The left-to-right (LR) waves have been filtered out in this map. (E) and (F) The Radon transformations of (C) and (D). Then We sum the absolute values of the data points in (E) and (F) along each column to get the solid lines in (G) and (H), respectively. The peaks identified on the lines give the optimal phase velocities of the LR and RL waves.

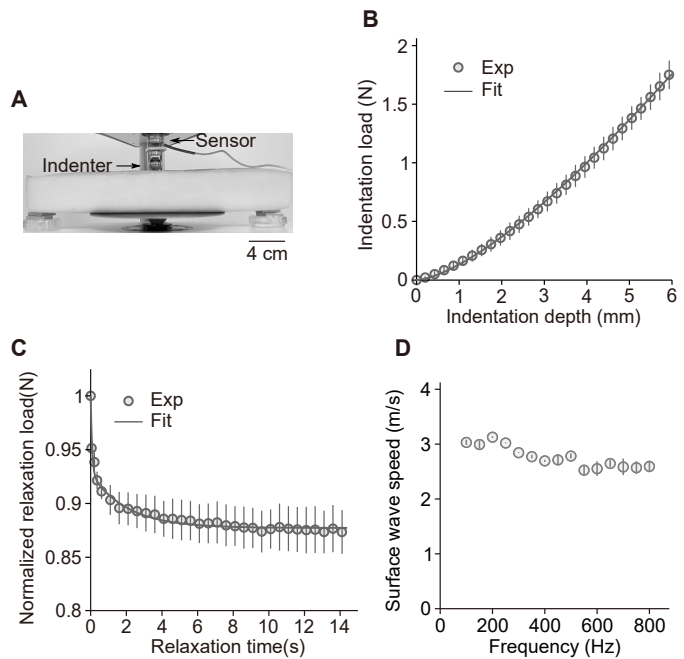


Fig. S5: Mechanical characterization of the hydrogel phantom at rest. (A) Photography showing the indentation tests on the hydrogel phantom. (B) Load-displacement curve of the indentation experiments obtained from the loading process with a low loading rate (~ 0.1 mm/s). Error bar, standard deviations over five measurements. (C) Normalized stress relaxation curve. Error bar: standard deviations over ten measurements. (D) Phase velocity of the surface waves.

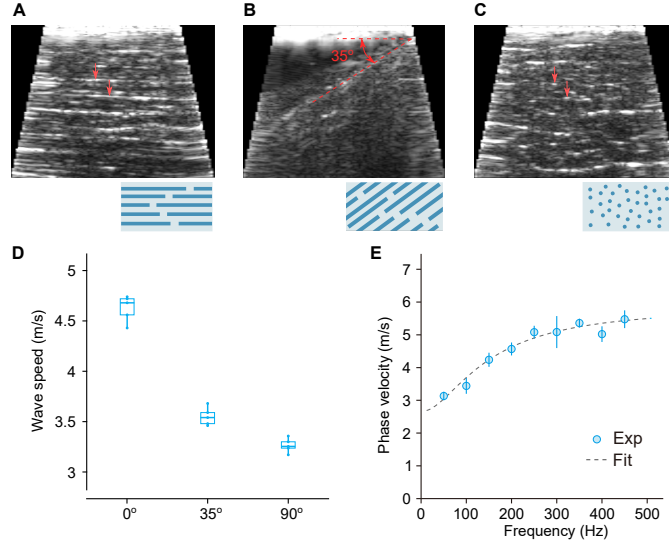


Fig. S6: Mechanical characterization of the skeletal muscle at rest. (A)-(C) Grayscale ultrasound images of the skeletal muscle. Red arrows in (A) and (C) indicate some of the parallel muscle fibers. For (B) the sample is tilted at $\sim 35^\circ$. The schematics underneath each image show the orientations of the muscle fibers. For all three cases, the horizontal shear wave group velocities v_x are measured. Therefore, the angles between the shear wave propagation direction and muscle fibers are (A) 0° , (B) 35° , and (C) 90° . (D) Statistical results (five independent measurements) for the horizontal shear wave group velocities. (E) Dispersion relation of the surface waves (0°). Markers, experiments. Dashed line, fitting curve obtained using one-term Prony series with $g_1 = 0.79$ and $\tau_1 = 0.49$ ms.

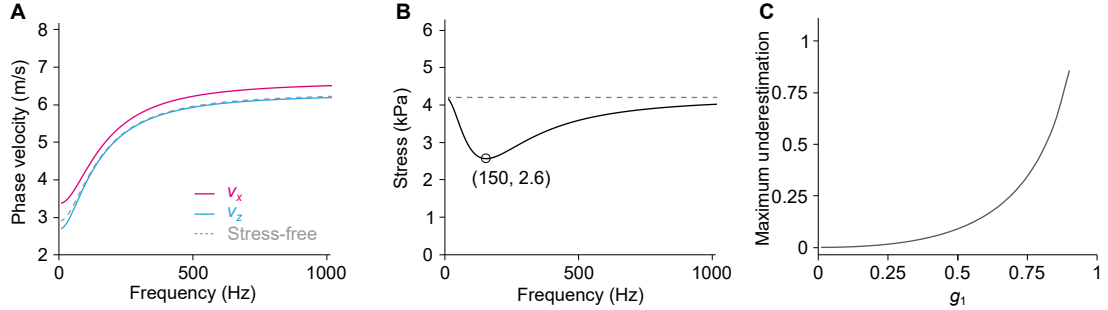


Fig. S7: Effect of viscoelasticity on the acoustoelastic imaging. (A) Dispersion relations of v_x and v_z when a tensile stress $\sigma_1 = 4.2$ kPa is applied. The dashed curve is the dispersion relation in the stress free state. The Quasi-Linear Viscoelastic material model used to produce this figure relies on the neo-Hookean model with $\mu_0 = 40$ kPa and the one-term Prony series with $g_1 = 0.79$ and $\tau = 0.49$ ms. (B) The stresses derived from v_x and v_z at different frequencies. The minimum stress is 2.6 kPa, indicating an underestimation of $\sim 38\%$. (C) The underestimation of the stress as a function of g_1 .

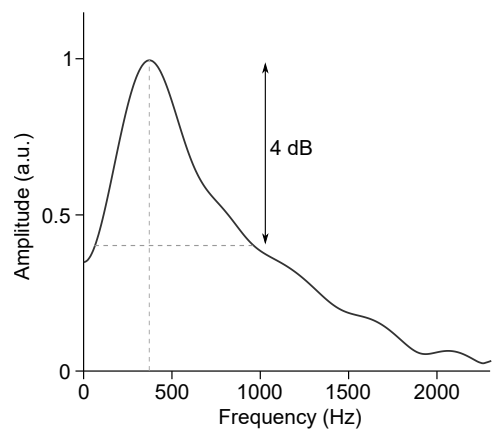


Fig. S8: A representative spectrum of the shear waves in the muscle sample. The central frequency is about 380 Hz and the 4dB bandwidth is about from 100 to 1,000 Hz.

Movie S1 (separate file). A movie given by finite element (FE) simulations compares the shear waves generated by programmed acoustic radiation force (ARF) and the conventional single ARF. (A) FE results of the shear waves generated by the programmed ARF; (B) FE results of the shear waves generated by a single ARF.

Movie S2 (separate file). A movie compares the shear waves generated in experiments by the programmed ARF and the conventional single ARF. (A) Experimental measurements of the shear waves generated by the programmed ARF; (B) Experimental measurements of the shear waves generated by a single ARF.

REFERENCES AND NOTES

1. N. L. Nerurkar, C. Lee, L. Mahadevan, C. J. Tabin, Molecular control of macroscopic forces drives formation of the vertebrate hindgut. *Nature* **565**, 480–484 (2019).
2. M. Gómez-González, E. Latorre, M. Arroyo, X. Trepat, Measuring mechanical stress in living tissues. *Nat. Rev. Phys.* **2**, 300–317 (2020).
3. K. H. Vining, D. J. Mooney, Mechanical forces direct stem cell behaviour in development and regeneration. *Nat. Rev. Mol. Cell Biol.* **18**, 728–742 (2017).
4. H. Ucar, S. Watanabe, J. Noguchi, Y. Morimoto, Y. Iino, S. Yagishita, N. Takahashi, H. Kasai, Mechanical actions of dendritic-spine enlargement on presynaptic exocytosis. *Nature* **600**, 686–689 (2021).
5. T. Tallinen, J. Y. Chung, F. Rousseau, N. Girard, J. Lefèvre, L. Mahadevan, On the growth and form of cortical convolutions. *Nat. Phys.* **12**, 588–593 (2016).
6. J.-H. Lee, H. S. Park, D. P. Holmes, Elastic instabilities govern the morphogenesis of the optic cup. *Phys. Rev. Lett.* **127**, 138102 (2021).
7. B. Li, F. Jia, Y.-P. Cao, X.-Q. Feng, H. Gao, Surface wrinkling patterns on a core-shell soft sphere. *Phys. Rev. Lett.* **106**, 234301 (2011).
8. S. K. Powers, M. J. Jackson, Exercise-induced oxidative stress: Cellular mechanisms and impact on muscle force production. *Physiol. Rev.* **88**, 1243–1276 (2008).
9. J. A. Martin, S. C. Brandon, E. M. Keuler, J. R. Hermus, A. C. Ehlers, D. J. Segalman, M. S. Allen, D. G. Thelen, Gauging force by tapping tendons. *Nat. Commun.* **9**, 1592 (2018).
10. J. Lee, S. J. Ihle, G. S. Pellegrino, H. Kim, J. Yea, C. Y. Jeon, H. C. Son, C. Jin, D. Eberli, F. Schmid, B. L. Zambrano, A. F. Renz, C. Forró, H. Choi, K. I. Jang, R. Küng, J. Vörös, Stretchable and suturable fibre sensors for wireless monitoring of connective tissue strain. *Nat. Electron.* **4**, 291–301 (2021).

11. J. Y. Sun, X. Zhao, W. R. Illeperuma, O. Chaudhuri, K. H. Oh, D. J. Mooney, J. J. Vlassak, Z. Suo, Highly stretchable and tough hydrogels. *Nature* **489**, 133–136 (2012).
12. J. Kim, G. Zhang, M. Shi, Z. Suo, Fracture, fatigue, and friction of polymers in which entanglements greatly outnumber cross-links. *Science* **374**, 212–216 (2021).
13. N. Matsuhisa, S. Niu, S. J. K. O'Neill, J. Kang, Y. Ochiai, T. Katsumata, H.-C. Wu, M. Ashizawa, G.-J. N. Wang, D. Zhong, X. Wang, X. Gong, R. Ning, H. Gong, I. You, Y. Zheng, Z. Zhang, J. B.-H. Tok, X. Chen, Z. Bao, High-frequency and intrinsically stretchable polymer diodes. *Nature* **600**, 246–252 (2021).
14. G. H. Lee, H. Moon, H. Kim, G. H. Lee, W. Kwon, S. Yoo, D. Myung, S. H. Yun, Z. Bao, S. K. Hahn, Multifunctional materials for implantable and wearable photonic healthcare devices. *Nat. Rev. Mater.* **5**, 149–165 (2020).
15. R. Bai, J. Yang, Z. Suo, Fatigue of hydrogels. *Eur. J. Mech. A/Solids* **74**, 337–370 (2019).
16. J. A. Rogers, T. Someya, Y. Huang, Materials and mechanics for stretchable electronics. *Science* **327**, 1603–1607 (2010).
17. Y. Wang, S. Lee, T. Yokota, H. Wang, Z. Jiang, J. Wang, M. Koizumi, T. Someya, A durable nanomesh on-skin strain gauge for natural skin motion monitoring with minimum mechanical constraints. *Sci. Adv.* **6**, eabb7043 (2020).
18. G. S. Schajer, Hole-drilling residual stress measurements at 75: Origins, advances, opportunities. *Exp. Mech.* **50**, 245–253 (2009).
19. N. S. Rossini, M. Dassisti, K. Y. Benyounis, A. G. Olabi, Methods of measuring residual stresses in components. *Mater. Des.* **35**, 572–588 (2012).
20. C. O. Ruud, A review of selected non-destructive methods for residual stress measurement. *NDT Int.* **15**, 15–23 (1982).

21. D. S. Hughes, J. L. Kelly, Second-order elastic deformation of solids. *Phys. Rev.* **92**, 1145 (1953).
22. A. N. Guz, F. G. Makhort, The physical fundamentals of the ultrasonic nondestructive stress analysis of solids. *Int. Appl. Mech.* **36**, 1119–1149 (2000).
23. F. Shi, J. E. Michaels, S. J. Lee, In situ estimation of applied biaxial loads with Lamb waves. *J. Acoust. Soc. Am.* **133**, 677–687 (2013).
24. J.-L. Gennisson, M. Rénier, S. Catheline, C. Barrière, J. Bercoff, M. Tanter, M. Fink, Acoustoelasticity in soft solids: Assessment of the nonlinear shear modulus with the acoustic radiation force. *J. Acoust. Soc. Am.* **122**, 3211–3219 (2007).
25. G.-Y. Li, A. Gower, M. Destrade, An ultrasonic method to measure stress without calibration: The angled shear wave method. *J. Acoust. Soc. Am.* **148**, 3963 (2020).
26. Y. Jiang, G. Y. Li, L. X. Qian, X. D. Hu, D. Liu, S. Liang, Y. Cao, Characterization of the nonlinear elastic properties of soft tissues using the supersonic shear imaging (SSI) technique: Inverse method, ex vivo and in vivo experiments. *Med. Image Anal.* **20**, 97–111 (2015).
27. C. Creton, C. Matteo, Fracture and adhesion of soft materials: A review. *Rep. Prog. Phys.* **79**, 046601 (2016).
28. M. Shams, M. Destrade, R. W. Ogden, Initial stresses in elastic solids: Constitutive laws and acoustoelasticity. *Wave Motion* **48**, 552–567 (2011).
29. A. L. Gower, T. Shearer, P. Ciarletta, A new restriction for initially stressed elastic solids. *Q. J. Mech. Appl. Math.* **70**, 455–478 (2017).
30. M. Destrade, M. D. Gilchrist, R. W. Ogden, Third-and fourth-order elasticities of biological soft tissues. *J. Acoust. Soc. Am.* **127**, 2103–2109 (2010).
31. C. Deroy, M. Destrade, A. Mc Alinden, A. Ní Annaidh, Non-invasive evaluation of skin tension lines with elastic waves. *Skin Res. Technol.* **23**, 326–335 (2017).

32. I. Hariton, G. Debottin, T. C. Gasser, G. A. Holzapfel, Stress-driven collagen fiber remodeling in arterial walls. *Biomech. Model. Mechanobiol.* **6**, 163–175 (2007).
33. G. W. Jones, S. J. Chapman, Modeling growth in biological materials. *SIAM Rev.* **54**, 52–118 (2012).
34. N. C. Rouze, A. Caenen, K. R. Nightingale, Phase and group velocities for shear wave propagation in an incompressible, hyperelastic material with uniaxial stretch. *Phys. Med. Biol.* **67**, 095015 (2022).
35. J. Bercoff, M. Tanter, M. Fink, Supersonic shear imaging: A new technique for soft tissue elasticity mapping. *IEEE Trans. Ultrason. Ferroelectr. Freq. Control* **51**, 396–409 (2004).
36. A. P. Sarvazyan, O. V. Rudenko, S. D. Swanson, J. B. Fowlkes, S. Y. Emelianov, Shear wave elasticity imaging: A new ultrasonic technology of medical diagnostics. *Ultrasound Med. Biol.* **24**, 1419–1435 (1998).
37. S. Catheline, N. Benech, Longitudinal shear wave and transverse dilatational wave in solids. *J. Acoust. Soc. Am.* **137**, EL200–EL205 (2015).
38. L. Sandrin, M. Tanter, J.-L. Gennisson, S. Catheline, M. Fink, Shear elasticity probe for soft tissues with 1-d transient elastography. *IEEE Trans. Ultrason. Ferroelectr. Freq. Control* **49**, 436–446 (2002).
39. L. Sandrin, D. Cassereau, M. Fink, The role of the coupling term in transient elastography. *J. Acoust. Soc. Am.* **115**, 73–83 (2004).
40. M. Tanter, M. Fink, Ultrafast imaging in biomedical ultrasound. *IEEE Trans. Ultrason. Ferroelectr. Freq. Control* **61**, 102–119 (2014).
41. N. C. Rouze, M. H. Wang, M. L. Palmeri, K. R. Nightingale, Robust estimation of time-of-flight shear wave speed using a radon sum transformation. *IEEE Trans. Ultrason. Ferroelectr. Freq. Control* **57**, 2662–2670 (2010).

42. J. P. Kerris, A. C. Betik, J. Li, G. K. McConell, Passive stretch regulates skeletal muscle glucose uptake independent of nitric oxide synthase. *J. Appl. Physiol.* **126**, 239–245 (2019).
43. B. Calvo, A. Ramírez, A. Alonso, J. Grasa, F. Soteras, R. Osta, M. J. Muñoz, Passive nonlinear elastic behaviour of skeletal muscle: Experimental results and model formulation. *J. Biomech.* **43**, 318–325 (2010).
44. J. P. Remenieras, M. Bulot, J. L. Gennisson, F. Patat, M. Destrade, G. Bacle, Acousto-elasticity of transversely isotropic incompressible soft tissues: Characterization of skeletal striated muscle. *Phys. Med. Biol.* **66**, 145009 (2021).
45. A. E. Knight, C. A. Trutna, N. C. Rouze, L. D. Hobson-Webb, A. Caenen, F. Q. Jin, M. L. Palmeri, K. R. Nightingale, Full characterization of in vivo muscle as an elastic, incompressible, transversely isotropic material using ultrasonic rotational 3D shear wave elasticity imaging. *IEEE Trans. Med. Imag.* **41**, 133–144 (2021).
46. H. Berjamin, R. De Pascalis, Acoustoelastic analysis of soft viscoelastic solids with application to pre-stressed phononic crystals. *Int. J. Solids Struct.* **241**, 111529 (2022).
47. G. Montaldo, M. Tanter, J. Bercoff, N. Benech, M. Fink, Coherent plane-wave compounding for very high frame rate ultrasonography and transient elastography. *IEEE Trans. Ultrason. Ferroelectr. Freq. Control* **56**, 489–506 (2009).
48. T. Loupas, J. Powers, R. W. Gill, An axial velocity estimator for ultrasound blood flow imaging, based on a full evaluation of the doppler equation by means of a two-dimensional autocorrelation approach. *IEEE Trans. Ultrason. Ferroelectr. Freq. Control* **42**, 672–688 (1995).
49. T. J. Hall, M. Bilgen, M. F. Insana, T. A. Krouskop, Phantom materials for elastography. *IEEE Trans. Ultrason. Ferroelectr. Freq. Control* **44**, 1355–1365 (1997).
50. R. W. Ogden, Incremental Statics and Dynamics of Pre-Stressed Elastic Materials. *Waves in Nonlinear Pre-Stressed Materials*, M. Destrade, G. Saccomandi, Eds. (Springer, Vienna, 2007), vol. 495, pp. 1–26.

51. G.-Y. Li, Y. Zheng, Y. Liu, M. Destrade, Y. Cao, Elastic Cherenkov effects in transversely isotropic soft materials-I: Theoretical analysis, simulations and inverse method. *J. Mech. Phys. Solids* **96**, 388–410 (2016).
52. M. Destrade, M. D. Gilchrist, G. Saccomandi, Third- and fourth-order constants of incompressible soft solids and the acousto-elastic effect. *J. Acoust. Soc. Am.* **127**, 2759–2763 (2010).
53. I. Tsvankin, *Seismic signatures and analysis of reflection data in anisotropic media* (Society of Exploration Geophysicists, 2012).
54. G.-Y. Li, Z.-Y. Zhang, J. Qian, Y. Zheng, W. Liu, H. Wu, Y. Cao, Mechanical characterization of functionally graded soft materials with ultrasound elastography. *Philos. Trans. A. Math. Phys. Eng. Sci.* **377**, 20180075 (2019).
55. J. G. Murphy, Transversely isotropic biological, soft tissue must be modelled using both anisotropic invariants. *Eur. J. Mech. A/Solids* **42**, 90–96 (2013).